Twofold $\mathcal{PT}$ symmetry in doubly exponential optical lattices

J. T. Cole,[1] K. G. Makris,[2,3] Z. H. Musslimani,[1] D. N. Christodoulides,[4] and S. Rotter[3]

[1]*Department of Mathematics, Florida State University, Tallahassee, Florida 32306, USA*

[2]*Physics Department, Crete Center for Quantum Complexity and Nanotechnology, University of Crete,
P.O. Box 2208, 71003 Heraklion, Greece*

[3]*Institute for Theoretical Physics, Vienna University of Technology, 1040 Vienna, Austria*

[4]*CREOL, College of Optics & Photonics, University of Central Florida, Orlando, Florida 32816, USA*

We introduce a family of non-Hermitian optical potentials that are given in terms of double-exponential periodic functions. The center of $\mathcal{PT}$ symmetry is not around zero and the potential satisfies a shifted $\mathcal{PT}$-symmetry relation at two distinct locations. Motivated by wave transmission through thin phase screens and gratings, we examine these refractive index modulations from the perspective of optical lattices that are homogeneous along the propagation direction. The diffraction dynamics, abrupt phase transitions in the eigenvalue spectrum, and exceptional points in the band structure are examined in detail. In addition, the nonlinear properties of wave propagation in Kerr nonlinearity media are studied. In particular, coherent structures such as lattice solitons are numerically identified by applying the spectral renormalization method. The spatial symmetries of such lattice solitons follow the shifted $\mathcal{PT}$-symmetric relations. Furthermore, such lattice solitons have a power threshold and their linear and nonlinear stabilities are critically dependent on their spatial symmetry point.

I. INTRODUCTION

One of the frontiers of modern photonics is the engineering of a complex refractive index to create new synthetic systems with novel functionalities. Nowadays it is understood that ideas and methods from quantum field theories and quantum mechanics [1,2] may be useful and applicable in such an engineering direction. A result of this fusion is the area of parity-time ($\mathcal{PT}$) -symmetric optics that originally started in the context of optical waveguide arrays and lattices [3–6]. After the first experimental observation of $\mathcal{PT}$-symmetry breaking, in a passive optical coupler [7] and in two coupled waveguides with gain and loss [8], this research area has attracted intense interest and attention, partially because of the possible applications in integrated photonics. In most technologies, such as photonic crystal fibers, metamaterials, and plasmonics, optical loss has always been considered an obstacle. However, it has recently been demonstrated that $\mathcal{PT}$-symmetric composite structures with balanced gain and loss distributions may offer an alternative solution to such technological problems. In fact, losses can be advantageous in various important applications such as optical isolators [9–13], coupled microring $\mathcal{PT}$-symmetric lasers [14,15], photonic molecules with exceptional points [16–18], $\mathcal{PT}$ metamaterials [19,20], $\mathcal{PT}$-symmetric plasmonics [21–23], and integrated silicon photonic structures [24,25].

All these findings in turn have stimulated much research activity in the general area of non-Hermitian and $\mathcal{PT}$ photonics and have led to several theoretical and experimental predictions. Examples include wave propagation and defect states in $\mathcal{PT}$ synthetic lattices [26–28], $\mathcal{PT}$-symmetry breaking in disordered lattices [29], linear [30] and nonlinear [31] beam dynamics close to the exceptional point, Hamiltonian formulation [32], soliton stability in $\mathcal{PT}$ lattices [33–36], Bloch oscillations, transport and localization in complex crystals [37], spectral singularities in non-Hermitian Friedrichs-Fano-Anderson models with complex potentials

[38], $\mathcal{PT}$-symmetric wave chaos [39], four-wave mixing [40], visualization of branch points in $\mathcal{PT}$-symmetric waveguides [41], subdiffraction and spatial filtering in media with gain and loss [42], unidirectional invisibility [43], scattering in $\mathcal{PT}$-symmetric optical cavities [44,45], dark solitons [46], transient amplification in lossy media [47], and constant intensity waves in linear and nonlinear optical systems [48].

In this paper we study linear and nonlinear wave propagation in a different type of optical lattice, that of a doubly exponential periodic potential. The transmission bands are computed using Floquet-Bloch theory and their physical properties are studied. We find a parameter regime (of the potential) corresponding to a high refractive index where the spectrum of the linear paraxial equation is entirely real. The linear beam dynamics of a wide class of Gaussian inputs is thoroughly investigated in the unbroken-$\mathcal{PT}$-symmetry phase. Finally, localized $\mathcal{PT}$-symmetric lattice solitons are numerically computed and their stability properties and nonlinear dynamics in the presence of noise are reported.

II. LATTICES WITH TWO $\mathcal{PT}$-SYMMETRY POINTS

The starting point of our analysis is the paraxial equation of diffraction [49], which governs the dynamic evolution of a linearly polarized scalar optical field $\psi(x,z)$ with a weakly guiding refractive index modulation $V(x)$ that is homogeneous in the propagation direction z. In one space dimension and in normalized units this is given by

$$i\psi_z + \psi_{xx} + V(x)\psi = 0. \tag{1}$$

Our physical motivation here is based on the wave scattering (in the context of the Helmholtz equation) of plane waves by non-Hermitian phase screens or gratings. Such a refractive index modulation is periodic and can be described by doubly exponential functions. The resulting diffraction pattern is spatially asymmetric due to the presence of gain and loss in the grating. In this paper we are interested in studying optical
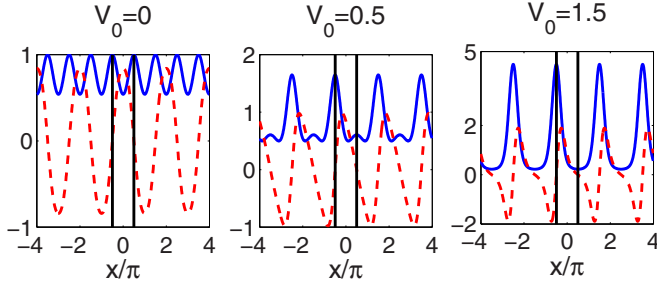
FIG. 1. Real (solid blue line) and imaginary (dashed red line) parts of the potential $V(x)$ given in Eq. (2) for different values of V_0. Vertical lines indicate the location of the symmetry points $x = \pm\pi/2$.

wave propagation in such photonic structures governed by Eq. (1). For this reason, we introduce the 2π-periodic doubly exponential potential

$$V(x) = e^{iW(x)}, \quad W(x) = \cos x + iV_0 \sin x, \quad (2)$$

with the free real parameter V_0, which, when split into its real and imaginary parts, yields

$$V(x) = e^{-V_0 \sin x}\cos(\cos x) + ie^{-V_0 \sin x}\sin(\cos x). \quad (3)$$

Interestingly enough, the potential $V(x)$ does not satisfy the usual symmetry relation $V^*(x) = V(-x)$. It rather satisfies the generalized twofold $\mathcal{PT}$-symmetry conditions

$$V^*(x) = V(\pi - x), \quad (4)$$

$$V^*(x) = V(-\pi - x). \quad (5)$$

As a consequence, the real and imaginary parts of $V(x)$ are, respectively, even and odd around the points $x = \pm\pi/2$. Thus the potential (2) possesses two distinct symmetry points. This is different from most studies on "standard" $\mathcal{PT}$-symmetric potentials (see [3,5]), which have focused on optical lattices with one symmetry point typically located at the origin. In Fig. 1 we show typical profiles of the lattice for various values of V_0. Depending on the magnitude of $|V_0|$, the real part of the potential admits two different local maxima (when $|V_0| < 1$) located exactly at the symmetry points $x = \pm\pi/2$ and their 2π-periodic extensions. On the other hand, for $|V_0| > 1$ the first symmetry point $x = -\pi/2 \pmod{2\pi}$ is now the only local maximum, whereas the other point now corresponds to a minimum.

At this point we comment on the physical meaning of V_0. In contrast to previous studies of $\mathcal{PT}$-symmetric optical lattices [3,5,6], where the potential parameter controls the level of gain and loss for a fixed real part of $V(x)$, here V_0 appears in both the real and imaginary parts of the optical potential. Thus changing V_0 would alter both the guiding index and the magnitude of the gain and loss. This can be clearly seen from Fig. 1. As V_0 increases, so does the distance between local maxima and the refractive index amplitude of the waveguides indicating a decrease in the coupling between adjacent channels. At the opposite limit, when $V_0 = 0$, the potential is $V(x) = e^{i\cos x}$.

III. BAND-STRUCTURE ANALYSIS AND DIFFRACTION DYNAMICS

A. Band structure and symmetry breaking

Before we consider the wave dynamics in such optical lattices, it is important to first understand their eigenvalue spectrum. In particular, we are interested in stationary solutions, or more precisely the Floquet-Bloch (FB) modes of the periodic index of refraction. We seek stationary solutions of the form $\psi(x,z) = \phi(x)e^{i\lambda z}$ in Eq. (1), which yield the linear eigenvalue problem

$$H\phi = \lambda\phi, \quad (6)$$

where $H = d^2/dx^2 + V(x)$ and λ is the propagation constant. Expanding the wave function ϕ using the partial wave method

$$\phi(x) = \sum_{n=-\infty}^{\infty} \hat{\phi}_n e^{i(k+n)x}, \quad (7)$$

with Bloch momentum k yields

$$\sum_m \hat{V}_m \hat{\phi}_{n-m} = [\lambda + (k+n)^2]\hat{\phi}_n, \quad n \in \mathbb{Z}, \quad (8)$$

where $\hat{V}_m$ are the Fourier coefficients of the potential given in closed form by

$$\hat{V}_m = C_m[1 + \operatorname{sgn}(m)V_0]^{|m|}\left(\frac{i}{2}\right)^{|m|}, \quad (9)$$

$$C_m = \frac{1}{|m|!} + \sum_{k=1}^{\infty}\left(\frac{i}{2}\right)^{2k}\frac{(1-V_0^2)^k}{k!(k+|m|)!}. \quad (10)$$

For a wide range of potential parameters V_0, the largest imaginary part of the eigenvalue λ as a function of k residing in the one-sided first Brillouin zone $[0, 1/2]$ has been computed. Depending on the magnitude of $|V_0|$, the spectrum can be completely real, partially complex, or fully complex. A summary of our findings is shown in Fig. 2. The parameter value $|V_0| = 1$ represents the exceptional point: For $|V_0| > 1$ the eigenvalues are all real and otherwise are complex. We note that for the well-known $\mathcal{PT}$ potential $V(x) = \cos(x) + iV_1 \sin(x)$ (see [3,5,6]) the spectrum is real only when $|V_1| < 1$.
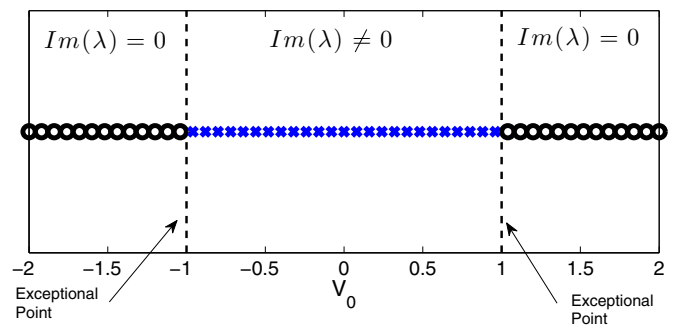

FIG. 2. Values of V_0 where the linear spectrum $\lambda(k)$ is broken or unbroken, where k is the Bloch momentum lying in the first Brillouin zone. Black circles indicate regimes where the linear spectrum is purely real [$\max |\operatorname{Im}\lambda(k)| \leqslant 10^{-8}$] and the blue crosses denote the zone where the spectrum is fully or partially complex.
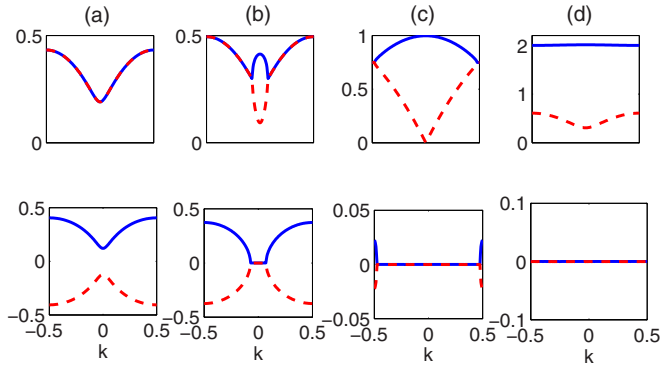
FIG. 3. First (solid blue line) and second (dashed red line) spectral bands corresponding to different values of V_0 below, at, and above the exceptional point. The top (bottom) row depicts the real (imaginary) part of the propagation constant λ as a function of the Bloch momentum k restricted to the first Brillouin zone. The depth of the potential V_0 is (a) 0.2, (b) 0.5, (c) 0.999, and (d) 1.5.

To further characterize the spectral properties of our potential and highlight its different structure, we next turn our attention to the band structure. To this end, we show in Fig. 3 the real and imaginary parts of the first two Floquet-Bloch bands corresponding to various values of V_0 below, at, and above the exceptional point. The geometric structure of the bands can be put into four distinct categories: (i) full overlap of the real part of the bands and opening of a global gap for their respective imaginary components [Fig. 3(a)], (ii) partial overlap of both real and imaginary bands as shown in Fig. 3(b) (both of these scenarios occur at potential strengths V_0 well below the exceptional point), (iii) the transition or exceptional point where the real bands intersect only at the edge of the Brillouin zone, whereas the corresponding imaginary parts coalesce to zero [Fig. 3(c)], and (iv) the opening of a global gap [Fig. 3(d)] above the exceptional point for which the entire spectrum is purely real.

One can intuitively explain the numerically observed spectral properties of H by using the imaginary shift relation [50,51]. By rewriting the potential $V(x)$ in the equivalent form

$$e^{iW(x)} = \begin{cases} e^{i\sqrt{1-V_0^2}\,\cos[x-i\tanh^{-1}(V_0)]}, & |V_0| < 1 \\ e^{ie^{ix}}, & |V_0| = 1 \\ e^{-\sqrt{V_0^2-1}\,\sin[x-i\tanh^{-1}(1/V_0)]}, & |V_0| > 1, \end{cases} \quad (11)$$

one can show that H is similar to

$$\mathcal{H} = \frac{d^2}{dx^2} + \exp[-\sqrt{V_0^2-1}\,\sin(x)], \quad (12)$$

when $|V_0| > 1$, i.e., $H = \exp(-\theta p)\mathcal{H}\exp(\theta p)$, where $\theta = -\tanh^{-1}(1/V_0)$ and $p = -i d/dx$. This result can be obtained by using the fact that $e^{-\theta p}xe^{\theta p} = x + i\theta$. Since the spectrum of $\mathcal{H}$ is real it implies, through the above similarity relation, that the spectrum of H is the same and also real. Note that at the exceptional point $|V_0| = 1$, the potential is described by the double-exponential function $V(x) = \exp[i\exp(ix)]$. We remark that in the case of a single-exponential function, i.e., $V(x) = \exp(ix)$, the eigenfunctions ϕ of Eq. (6) are exactly Bessel beams [33].
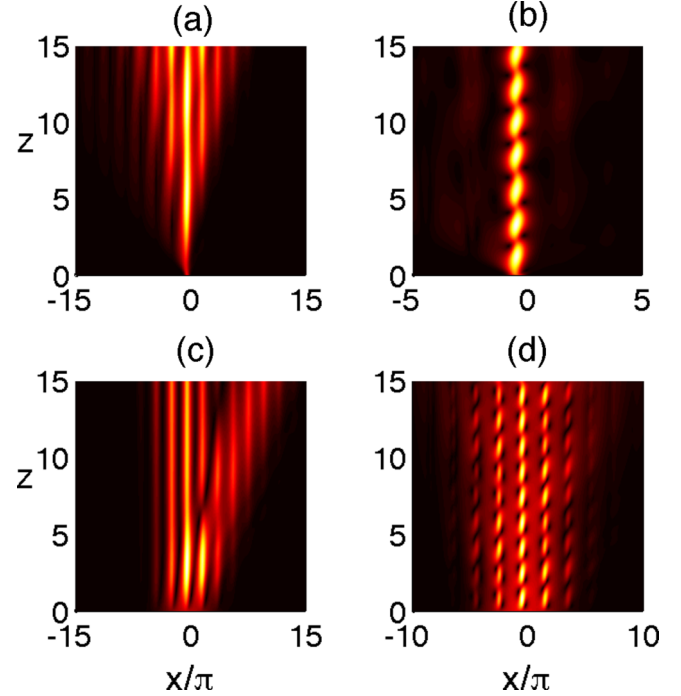

FIG. 4. Linear evolution of optical field $|\psi(x,z)|$ obtained from Eq. (1) subject to initial conditions (a) and (b) $\psi(x,0) = e^{-(x+\pi/2)^2}$ and (c) and (d) $\psi(x,0) = e^{-.01(x+\pi/2)^2}$ with potential parameters (a) and (c) $V_0 = 1$ and (b) and (d) $V_0 = 2$.

B. Beam diffraction dynamics

In this section we are interested in exploring the linear dynamic behavior of various input Gaussian beams in the presence of a doubly exponential lattice with unbroken $\mathcal{PT}$ symmetry. In this regard, we consider two important cases $V_0 = 1$ and $V_0 = 2$. In the latter, the lattice is relatively large, corresponding to a high refractive index and well-separated potential wells. Thus, the dynamics of a narrow input Gaussian beam centered at $x = -\pi/2$ (a global maximum point of the lattice) yields a wave pattern that is well confined. On the other hand, the same input wave would diffract if the refractive index were lowered, as one can see from Figs. 4(a) and 4(b). The situation is different when one instead considers wide input Gaussian beams. For example, in the shallow lattice limit, a double refraction pattern is observed [see Fig. 4(c)], whereas for higher lattice potentials power oscillations occur over many sites.

At this point we note that for the cases of a broad input Gaussian beam [Figs. 4(c) and 4(d)] the diffraction pattern is less sensitive to the location of the beam's center because the distribution of its projection coefficients is less localized in the Brillouin zone. On the other hand, for a narrow Gaussian profile [Figs. 4(a) and 4(b)], the diffraction patterns are different depending on the location of the beam's center ($x = 0$, $\pi/2$, or $-\pi/2$). In particular, the asymmetries of the diffraction patterns in Fig. 4 can be further analyzed and explained by projecting the initial beam at $z = 0$ [6]. By using the biorthogonality relations of the nonorthogonal Floquet-Bloch modes, one can understand from the distribution of the beam's projection coefficients over all the bands in the
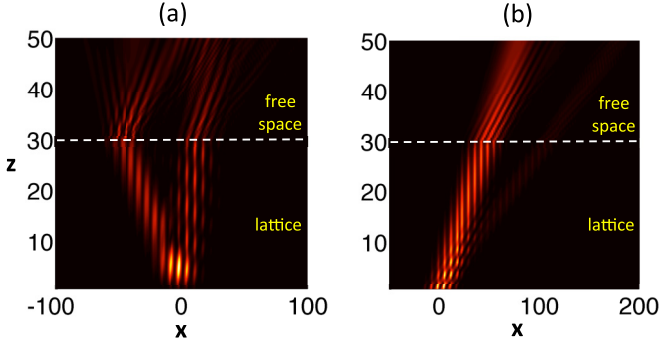
FIG. 5. Intensity diffraction pattern of an incident wide Gaussian beam subject to initial conditions (a) $\psi(x,0) = e^{-(x/15)^2 - i0.8x}$ and (b) $\psi(x,0) = e^{-(x/15)^2 + i0.8x}$ with the potential parameter $V_0 = 1.01$. Note that, in both (a) and (b), the lattice is switched off at $z = 30$ and the beam propagates in free space for $z > 30$.

Brillouin zone the resulting diffraction pattern. Another factor that one has to take into account is the dependence of coupling on the parameter V_0. The difference between the two cases is that in Fig. 4(a) ($V_0 = 1$) the wave coupling is higher than that shown in Fig. 4(b) ($V_0 = 2$). Therefore, in the first case there is coupling between adjacent channels (asymmetric diffraction to the left), while in the latter case the light is trapped mostly in one waveguide by losing energy to radiation losses. Since the modes of any individual waveguide have tilted phase fronts (from left to right) the diffraction pattern would be asymmetric to the right, as one can see in Fig. 4.

Many of the diffraction characteristics (double refraction, power oscillations, etc.) of wide Gaussian beams are generic in parity-time-symmetric periodic potentials and are a direct outcome of the mode nonorthogonality. In particular, since there is gain and loss in the refractive index transverse modulation, the phase fronts of the FB modes are tilted. This phase front tilt is related to the nonzero transverse Poynting vector flow and has observable consequences in the beam's diffraction. In order to better understand this factor, we examine (see Fig. 5) the wave dynamics of a wide Gaussian beam in the presence of a doubly exponential $\mathcal{PT}$ lattice that is turned off after the beam has propagated some finite distance Z (here $Z = 30$). Thus, for $z \geqslant Z$ there is no optical potential and the beam diffracts in free space. More specifically, we consider incident beams tilted to the left [Fig. 5(a)] and to the right [Fig. 5(b)] at $z = 0$. Due to the skewness of the involved FB modes, the beam undergoes a "negative" type of refraction (breaking Snell's law) that is directly observable in the case of incidence from the left side [Fig. 5(a)].

At this point we note that Figs. 4 and 5 highlight different physical phenomena. The former figure displays the double refraction and power oscillations inside the medium, while the latter figure shows what happens to a beam at the interface between lattice and free space (negative refraction). Furthermore, the beams in Fig. 4 propagate at normal incidence, while those in Fig. 5 are coupled to the lattice on an angle (oblique incidence). The effect of the beam width and centering on the tilted beam diffraction dynamics is a nontrivial issue, however it can be systematically understood by projecting the initial Gaussian beam to the biorthogonal FB eigenbasis [6].

Moreover, the closer the value V_0 is to the exceptional point, the higher the degree of non-Hermiticity becomes. This non-Hermitian character (combined with the interference between nonorthogonal FB modes) leads to the complex diffraction patterns described in Figs. 4 and 5, i.e., power oscillations, asymmetric wave transport, and negative refraction.

IV. NONLINEAR COHERENT STRUCTURES IN DOUBLY EXPONENTIAL POTENTIALS

A. Power-eigenvalue curves and lattice solitons

Having studied the linear properties of the potential and linear wave dynamics, we next focus our attention on nonlinear wave propagation in the presence of a doubly exponential lattice. The governing equation is the one-dimensional normalized nonlinear Schrödinger equation

$$i\psi_z + \psi_{xx} + V(x)\psi + |\psi|^2\psi = 0. \qquad (13)$$

In particular, we are interested in the structure of lattice solitons and their nonlinear dynamics subject to perturbative noise. To this end, we consider stationary waveguide solutions of the form $\psi(x,z) = \phi(x)\exp(i\lambda z)$, which yield

$$\phi_{xx} + V(x)\phi + |\phi|^2\phi = \lambda\phi, \qquad (14)$$

for the complex localized eigenmode ϕ and real propagation constant λ. Since Eq. (14) admits two $\mathcal{PT}$-symmetry points $x = \pm\pi/2$, this in turn induces two different families of solutions, which here we refer to as $\phi_{\pm}$. Furthermore, they satisfy the $\mathcal{PT}$-symmetry condition

$$\int_{-\infty}^{\infty} \text{Im}\{V(x)\}|\phi_{\pm}(x)|^2 dx = 0. \qquad (15)$$

We consider nonlinear localized modes whose propagation constants λ are real and reside in the semi-infinite gap, as well as potential parameters corresponding to both broken ($|V_0| < 1$) and unbroken ($|V_0| > 1$) $\mathcal{PT}$ symmetries. Band-gap lattice solitons in a single-exponential $\mathcal{PT}$-symmetric potential have been studied along with with their stability properties [33]. We note that when the $\mathcal{PT}$ symmetry is no longer exact the linear spectrum can be partially complex, in which case lattice solitons still exist. Such a scenario has been reported in [5] for a single-exponential potential. Typical soliton solutions obtained by the spectral renormalization method [52] or Newton conjugate-gradient scheme [53] are shown in Fig. 6 along with the guiding index potential. The ϕ_- family is centered at a global lattice maximum (high refractive index) with a dominant peak as well as all remaining humps located at global maxima of the index profile. The solution depicted in Fig. 6(a) is obtained for $V_0 = 0.5$ where the $\mathcal{PT}$ symmetry is broken, whereas the one shown in Fig. 6(c) corresponds to an exact linear $\mathcal{PT}$ symmetry. In both cases, the real and imaginary parts of the wave function ϕ_- are even and odd, respectively, around $x = -\pi/2$. To further characterize this family, we have computed the power curves defined by

$$P(\lambda,V_0) = \int_{-\infty}^{\infty} |\phi_{\pm}(x,\lambda,V_0)|^2 dx, \qquad (16)$$

for a wide range of potential values and soliton propagation constants, both when the $\mathcal{PT}$ symmetry is broken and when it
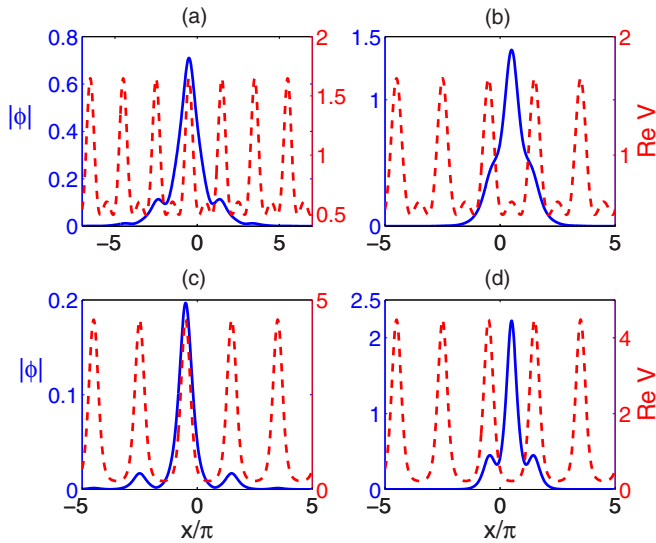
FIG. 6. Gap solitons obtained from Eq. (14) (solid blue line) along with the real part of the lattice potential (dashed red line) for the parameters (a) $V_0 = 0.5$ and $\lambda = 0.76$, (b) $V_0 = 0.5$, $\lambda = 1.36$, (c) $V_0 = 1.5$ and $\lambda = 2.04$, and (d) $V_0 = 1.5$ and $\lambda = 2.71$.

is exact. The results are summarized in Fig. 7(a). In the shallow lattice limit, there is a minimum optical power necessary to generate a fundamental lattice soliton. Increasing the potential amplitude produces a higher effective refractive index at the
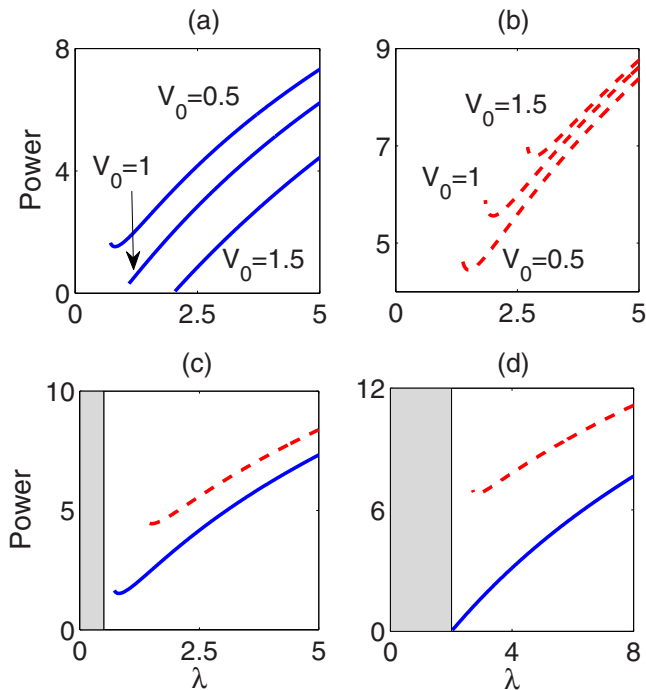

FIG. 7. Power curves [see Eq. (16)] for solitons with eigenvalues located in the semi-infinite gap centered at (a) $x = -\pi/2$ and (b) $x = \pi/2$. For comparison, the existence curves of both families at fixed potential depths (c) $V_0 = 0.5$ and (d) $V_0 = 1.5$ are shown along side each other. The dashed red and solid blue lines represent the ϕ_+ and ϕ_- families, respectively.

left symmetry point, thus decreasing the amount of power needed to support the formation of such nonlinear modes.

Next we study the other localized family ϕ_+, which could be centered around either a local lattice maximum or minimum depending on the value of $|V_0|$. Prototypical soliton examples are shown in Figs. 6(b) and 6(d) with main peaks located at the right $\mathcal{PT}$-symmetry point and remaining humps at adjacent potential maxima. The corresponding existence curves for several V_0 are shown in Fig. 7(b). Interestingly enough, for a fixed real soliton eigenvalue, solutions have higher power as $|V_0|$ increases (the opposite of the scenario encountered in the ϕ_- family). This is due to the fact that as $|V_0|$ increases the potential shape changes, which in turn forces the soliton to center at a potential minimum, rather than at a local maximum. Moreover, each of these solutions displays a power threshold necessary to generate a fundamental lattice soliton.

Up until now we have considered the $\phi_\pm$ families individually, i.e., they were grouped according to their symmetry points. Now we examine their structural properties from a different point of view, namely, we fix the potential depth V_0 and examine the soliton power for both families as λ is varied. The results are shown in Figs. 7(c) and 7(d). The solutions centered at the global maxima are observed to have lower power than their counterparts (the ϕ_+ solutions) and, at a fixed eigenvalue λ, the difference in the soliton power curves grow with increasing $|V_0|$. We note that in the higher refractive index regime, the lower branch continues all the way to the (real) linear spectral boundary [see Fig. 7(d)]. Finally, we point out that lattice solitons with power thresholds have been previously studied and identified in another context, that of the so-called surface solitons [54,55]. In this case, the optical potential is Hermitian and the soliton solutions exist at the boundary between the lattice and the bulk. The existence of a termination surface leads to a power threshold.

B. Linear and nonlinear stability analysis

In this section we turn our attention to study linear and nonlinear stability properties of the $\phi_\pm$ lattice solitons found above. Our approach is based on numerically solving the corresponding linear stability equation combined with direct numerical simulations. To do so, we consider perturbations on solutions to Eq. (13) of the form

$$\psi(x,z) = [\phi_\pm(x) + \eta(x,z)]e^{i\lambda z}, \qquad (17)$$

where the perturbation η is assumed to be small in comparison to the soliton size. With this in mind, linearizing around the solutions $\phi_\pm(x)$ gives

$$i\eta_z - \lambda\eta + \eta_{xx} + V(x)\eta + \phi_\pm^2\eta^* + 2|\phi_\pm|^2\eta = 0. \quad (18)$$

Equation (18) governs the evolution of the perturbation $\eta(x,z)$ subject to localized initial and boundary conditions. To fully address the linear stability problem we consider two approaches, each of which provides its own insight into the linear stability properties. First, we integrate Eq. (18) directly for some noisy initial data and monitor the field intensity over many realizations. Physically speaking, this scenario is commonly encountered in experiments where localized noise serves as the main source of perturbations. Second, we assume that the perturbation grows exponentially in the propagation

distance and obtain a spectral linear stability problem, which is then numerically solved for the perturbation eigenvalues. The latter gives a global picture of the stability development.

To this end, the soliton is initially perturbed by a wide Gaussian beam seeded with random amplitude of the form

$$\eta(x, z = 0) = Ar(x)e^{-x^2/10}, \qquad (19)$$

where A is a constant chosen to gauge the perturbation magnitude relative to the soliton peak. The function $r(x)$ is a complex-valued random field constructed using spectral filtering [56], i.e.,

$$r(x) = \mathcal{F}^{-1}[e^{-\xi^2/4}\mathcal{F}[\tilde{r}_1(x) + i\tilde{r}_2(x)](\xi)], \qquad (20)$$

where $\tilde{r}_{1,2}(x)$ are real random fields normally distributed on the whole real line with mean zero and unit standard deviation. The forward and inverse Fourier transforms are given, respectively, by

$$\mathcal{F}[f] = \frac{1}{\sqrt{2\pi}} \int_{-\infty}^{\infty} f(x)e^{-i\xi x}dx, \qquad (21)$$

$$\mathcal{F}^{-1}[\hat{f}] = \frac{1}{\sqrt{2\pi}} \int_{-\infty}^{\infty} \hat{f}(\xi)e^{i\xi x}d\xi. \qquad (22)$$

Throughout the rest of the paper, the amplitude is fixed to be $A = 0.05 \max|\phi_\pm|/\max|r|$. Equation (18) is numerically integrated using a spectral Runge-Kutta scheme.

We first comment on the ϕ_- family. The numerical simulations shown in Fig. 8(a) reveal that when the linear $\mathcal{PT}$ symmetry is broken, perturbations grow unboundedly,

driving the soliton to become unstable. In some sense, this result is expected since the linear spectrum of eigenvalue problem (6) is now partially or fully complex. The situation is drastically different for solitons whose propagation constants correspond to exact $\mathcal{PT}$ symmetry. As one can see from Fig. 8(c), the soliton develops a very weak instability. The stability properties of the ϕ_+ family share many common features with those of the ϕ_- family. That is to say, below the exceptional point, the instability develops at a growth rate comparable to that of the ϕ_- family [see Fig. 8(b)]. The main distinction, as shown in Fig. 8(d), happens above the exceptional point, where now the instability is orders of magnitude larger than the one observed in the ϕ_- mode. Thus, semi-infinite gap modes centered at $x = -\pi/2$, or at a global potential maximum, corresponding to real soliton propagation constants are less unstable [against the random perturbation given in Eq. (19)] than those centered at $x = \pi/2$.

To supplement the above linear stability findings, we next consider a specific type of perturbations that grow exponentially in z, i.e.,

$$\eta(x, z) = F(x)e^{\mu z} + G^*(x)e^{\mu^* z}, \qquad (23)$$

where F and G are complex-valued eigenfunctions assumed to be localized in x. Substituting this ansatz into Eq. (18) yields the eigenvalue system

$$i\begin{pmatrix} \hat{L} & \phi^2 \\ -(\phi^*)^2 & -\hat{L}^* \end{pmatrix}\begin{pmatrix} F \\ G \end{pmatrix} = \mu\begin{pmatrix} F \\ G \end{pmatrix}, \qquad (24)$$

where $\hat{L} = -\lambda + d^2/dx^2 + V(x) + 2|\phi|^2$ and $\hat{L}^*$ is the adjoint of $\hat{L}$ in the space of square-integrable functions. Solutions
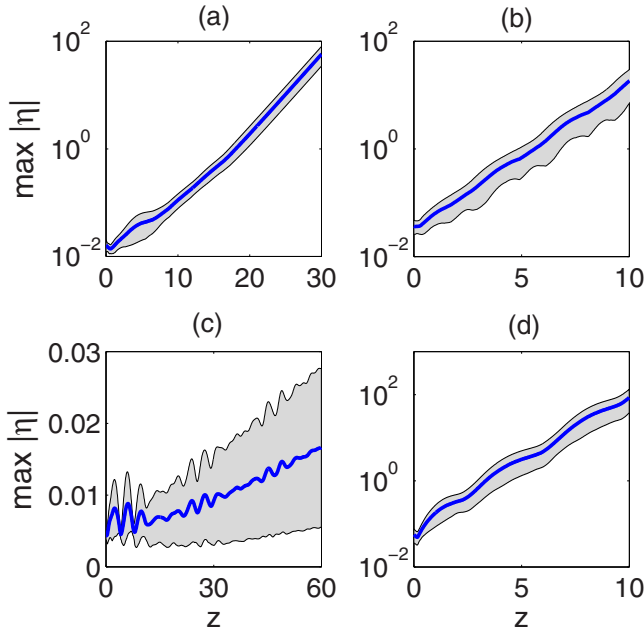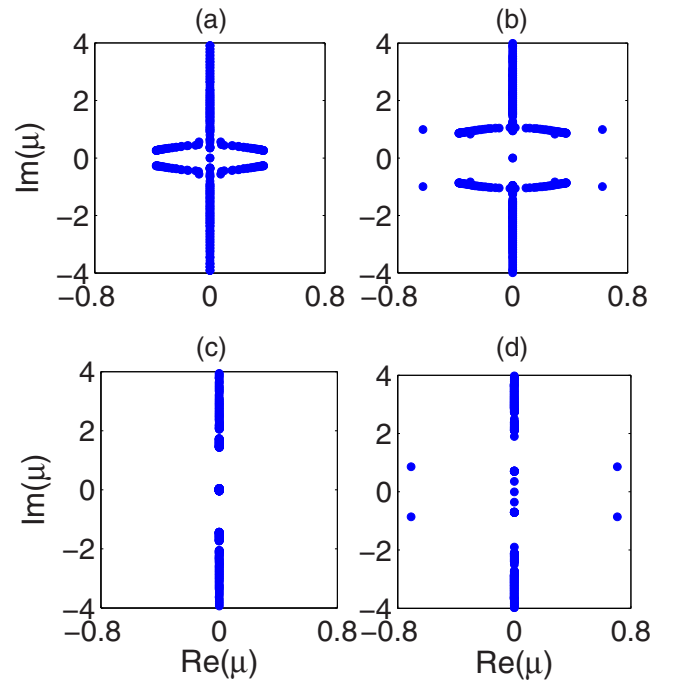

FIG. 8. Evolution of the maximum value of the perturbation averaged over ten realizations of randomness obtained from Eq. (18) with the initial condition (19). The gray area designates the standard deviation away from the mean. The left and right columns correspond, respectively, to the ϕ_- and ϕ_+ families. The parameters are (a) $V_0 = 0.5$ and $\lambda = 0.76$, (b) $V_0 = 0.5$ and $\lambda = 1.36$, (c) $V_0 = 1.5$ and $\lambda = 2.04$, and (d) $V_0 = 1.5$ and $\lambda = 2.71$.

FIG. 9. Spectrum of eigenvalue problem (24). The left and right columns correspond, respectively, to the ϕ_- and ϕ_+ families. The parameters are (a) $V_0 = 0.5$ and $\lambda = 0.76$, (b) $V_0 = 0.5$ and $\lambda = 1.36$, (c) $V_0 = 1.5$ and $\lambda = 2.04$, and (d) $V_0 = 1.5$ and $\lambda = 2.71$.

corresponding to the eigenvalue problem (24) with $\mathrm{Re}(\mu) \neq 0$ are said to be linearly unstable. To determine the unstable spectrum, we solve eigenvalue system (24) using Fourier [57] collocation methods and differentiation matrices [58]. The resulting stability spectra are shown in Fig. 9. Regardless of the soliton symmetry point, nonlinear modes obtained in the broken $\mathcal{PT}$-symmetry regime are found to be linearly unstable [see Figs. 9(a) and 9(b)]. These findings are consistent with the results obtained in Figs. 8(a) and 8(b). On the other hand, the linearized stability spectrum for the ϕ_- family is located entirely on the imaginary axis [see Fig. 9(c)] for V_0 values above the exceptional point, hence they are neutrally stable. It is worth mentioning that the very same soliton solution developed weak instabilities against random localized perturbations over very long distances in Fig. 8(c). We note that the stability properties for the ϕ_- family resemble those of the fundamental solutions considered in [5,33]. Finally, the ϕ_+ representatives are also observed to be unstable since the stability eigenvalues μ are complex. This scenario concurs with the numerical linear stability problem encountered in Fig. 8(d).

Up until now we have studied the stability properties of localized modes against small random localized perturbations as well as exponentially growing (in z) perturbation eigenfunctions. To deviate from that linear regime, we next examine the nonlinear dynamics of lattice solitons under the action of a localized random perturbation. Equation (13) is numerically solved using a spectral fourth-order Runge-Kutta method with localized boundary conditions and an input beam given by

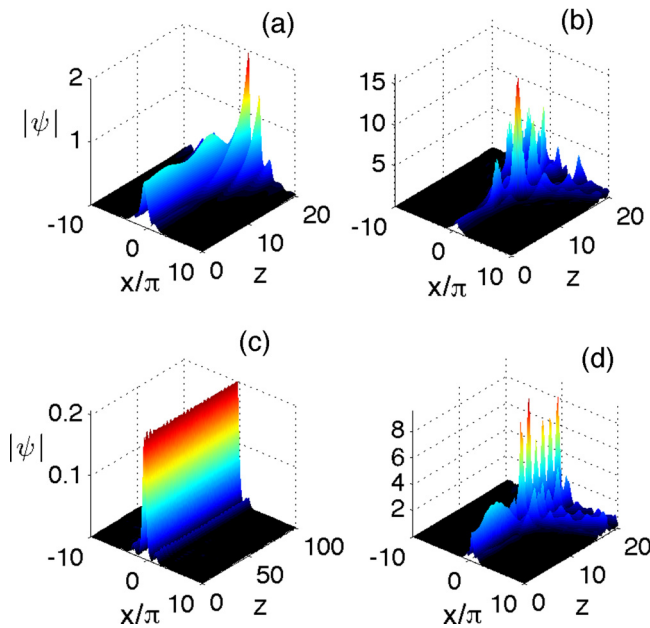$$\psi(x,z=0) = \phi_\pm(x) + Ar(x)e^{-x^2/10}, \qquad (25)$$

FIG. 10. Soliton nonlinear dynamics obtained from Eq. (13) subject to the initial condition given by Eq. (25). Shown are representations of the evolution profile of the wave amplitude as a function of x and z for (a) and (c) the ϕ_- family and (b) and (d) the ϕ_+ family. The parameters are (a) $V_0 = 0.5$ and $\lambda = 0.76$, (b) $V_0 = 0.5$ and $\lambda = 1.36$, (c) $V_0 = 1.5$ and $\lambda = 2.04$, and (d) $V_0 = 1.5$ and $\lambda = 2.71$.
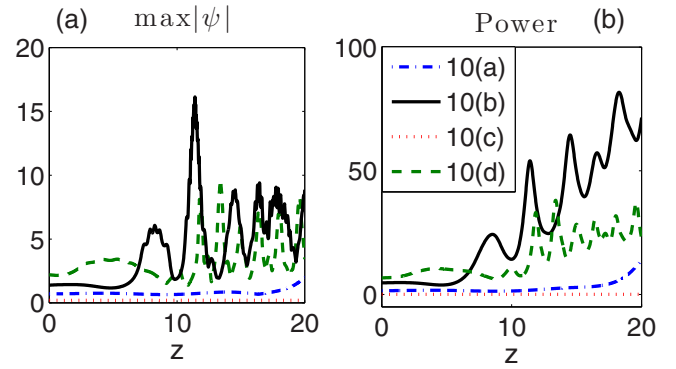

FIG. 11. Dynamic evolution of the (a) maximum peak and (b) total power corresponding to the direct numerical simulations shown in Fig. 10.

where A and $r(x)$ are the same as in Eq. (19). Typical numerical results are shown in Fig. 10. Overall, the nonlinear stage of the perturbation evolution seems to preserve the stability picture reported earlier. That is to say, the ϕ_+ family is nonlinearly unstable regardless of the guiding index depth. To visualize the development (or lack thereof) of the nonlinear instability, we present in Figs. 11(a) and 11(b) the maximum peak and total power of the beam as a function of z, respectively. The measured soliton peak amplitude and power exhibit growing oscillatory behavior. The story with the ϕ_- family is quite different. In the unbroken $\mathcal{PT}$ phase, the solitons are dynamically stable over long propagation distances with small and controlled oscillations superimposed on top of the beam [see Fig. 10(c)]. We would like to point out that, in this parameter regime, a low-amplitude Gaussian input beam was also found to support an almost-diffraction-free propagation for sufficiently large lattice depth [see Fig. 4(b)]. Recall as well that in the linear stability analysis only the ϕ_- family with $|V_0| > 1$ grew at a less than exponential rate with a linear stability spectrum [obtained from Eq. (24)] lying entirely on the imaginary axis [see Fig. 9(c)]. However, for different members of the same family, the peak amplitude grows rapidly with z when $|V_0| < 1$ [Fig. 10(a)].

V. CONCLUSION

In the context of $\mathcal{PT}$-symmetric optics, we examined the spectral properties of a different class of non-Hermitian periodic potentials, namely, that of coupled waveguides, represented by a double-exponential periodic function. In particular, the complex refractive index distributions are given by $V(x) = e^{iW(x)}$, where $W(x) = \cos(x) + iV_0 \sin(x)$. Unlike most optical $\mathcal{PT}$ refractive indices, whose $\mathcal{PT}$ symmetry is usually given at one point, this class of optical structures satisfies a shifted twofold $\mathcal{PT}$ symmetry around $x = \pm\pi/2$. It is found that the linear spectrum associated with these potentials is entirely real for $|V_0| > 1$ and exceptional points characterize this abrupt phase transition from broken to unbroken shifted $\mathcal{PT}$ symmetry. The effect of the FB-mode phase front tilt in the diffraction dynamics was also examined. Our analysis was extended to the nonlinear (self-focusing) regime where lattice solitons were found to exist above a specific power threshold for certain parameters. The center of spatial symmetry of such solitons coincides with the shifted $\mathcal{PT}$-symmetry points. The linear and nonlinear dynamic stabilities of these lattice

solitons were investigated by direct numerical simulations and by solving a stability eigenvalue problem. The solitons in the unbroken-$\mathcal{PT}$-symmetry regime can be stable depending on their spatial point of symmetry.

ACKNOWLEDGMENTS

[1] C. M. Bender and S. Boettcher, Phys. Rev. Lett. **80**, 5243 (1998).

[2] C. M. Bender, Rep. Prog. Phys. **70**, 947 (2007).

[3] K. G. Makris, R. El-Ganainy, D. N. Christodoulides, and Z. H. Musslimani, Phys. Rev. Lett. **100**, 103904 (2008).

[4] R. El-Ganainy, K. G. Makris, D. N. Christodoulides, and Z. H. Musslimani, Opt. Lett. **32**, 2632 (2007).

[5] Z. H. Musslimani, K. G. Makris, R. El-Ganainy, and D. N. Christodoulides, Phys. Rev. Lett. **100**, 030402 (2008).

[6] K. G. Makris, R. El-Ganainy, D. N. Christodoulides, and Z. H. Musslimani, Phys. Rev. A **81**, 063807 (2010).

[7] A. Guo, G. J. Salamo, D. Duchesne, R. Morandotti, M. Volatier-Ravat, V. Aimez, G. A. Siviloglou, and D. N. Christodoulides, Phys. Rev. Lett. **103**, 093902 (2009).

[8] C. E. Rüter, K. G. Makris, R. El-Ganainy, D. N. Christodoulides, M. Segev, and D. Kip, Nat. Phys. **6**, 192 (2010).

[9] H. Ramezani, T. Kottos, R. El-Ganainy, and D. N. Christodoulides, Phys. Rev. A **82**, 043803 (2010).

[10] N. Bender, S. Factor, J. D. Bodyfelt, H. Ramezani, D. N. Christodoulides, F. M. Ellis, and T. Kottos, Phys. Rev. Lett. **110**, 234101 (2013).

[11] F. Nazari, N. Bender, H. Ramezani, M. K. Moravvej-Farshi, D. N. Christodoulides, and T. Kottos, Opt. Express **22**, 9574 (2014).

[12] L. Chang, X. Jiang, S. Hua, C. Yang, J. Wen, L. Jiang, G. Li, G. Wang, and M. Xiao, Nat. Photon. **8**, 524 (2014).

[13] B. Peng, S. K. Özdemir, F. Lei, F. Monifi, M. Gianfreda, G. L. Long, S. Fan, F. Nori, C. M. Bender, and L. Yang, Nat. Phys. **10**, 394 (2014).

[14] H. Hodaei, M.-A. Miri, M. Heinrich, D. N. Christodoulides, and M. Khajavikhan, Science **346**, 975 (2014).

[15] L. Feng, Z. J. Wong, R.-M. Ma, Y. Wang, and X. Zhang, Science **346**, 972 (2014).

[16] M. Liertzer, L. Ge, A. Cerjan, A. D. Stone, H. E. Türeci, and S. Rotter, Phys. Rev. Lett. **108**, 173901 (2012).

[17] M. Brandstetter, M. Liertzer, C. Deutsch, P. Klang, J. Schöbert, H. E. Türeci, G. Strasser, K. Unterrainer, and S. Rotter, Nat. Commun. **5**, 4034 (2014).

[18] B. Peng, S. K. Ozdemir, S. Rotter, H. Yilmaz, M. Liertzer, F. Monifi, C. M. Bender, F. Nori, L. Yang, Science, **346**, 328 (2014).

[19] N. Lazarides and G. P. Tsironis, Phys. Rev. Lett. **110**, 053901 (2013).

[20] G. Castaldi, S. Savoia, V. Galdi, A. Alu, and N. Engheta, Phys. Rev. Lett. **110**, 173901 (2013).

[21] J. Ctyrosky, V. Kuzmiak, and S. Eyderman, Opt. Express **18**, 21585 (2010).

[22] H. Benisty, A. Degiron, A. Lupu, A. De Lustrac, S. Chénais, S. Forget, M. Besbes, G. Barbillon, A. Bruyant, S. Blaize, and G. Lérondel, Opt. Express **19**, 18004 (2011).

[23] A. Lupu, H. Benisty, and A. Derigon, Opt. Express **21**, 21651 (2013).

[24] L. Feng, M. Ayache, J. Huang, Y.-L. Xu, M.-H. Lu, Y.-F. Chen, Y. Fainman, and A. Scherer, Science **333**, 729 (2011).

[25] L. Feng, Y.-L. Xu, W. S. Fegadolli, M.-H. Lu, J. E. B. Oliveira, V. R. Almeida, Y.-F. Chen, and A. Scherer, Nat. Mater. **12**, 108 (2013).

[26] A. Regensburger, C. Bersch, M. A. Miri, G. Onishchukov, D. N. Christodoulides, and U. Peschel, Nature (London) **488**, 167 (2012).

[27] A. Regensburger, M. A. Miri, C. Bersch, J. Näger, G. Onishchukov, D. N. Christodoulides, and U. Peschel, Phys. Rev. Lett. **110**, 223902 (2013).

[28] P. G. Kevrekidis, D. E. Pelinovsky, and D. Tyugin, SIAM J. Appl. Dyn. Syst. **12**, 1210 (2013).

[29] O. Bendix, R. Fleischmann, T. Kottos, and B. Shapiro, Phys. Rev. Lett. **103**, 030402 (2009).

[30] M. Turduev, M. Botey, I. Giden, R. Herrero, H. Kurt, E. Ozbay, and K. Staliunas, Phys. Rev. A **91**, 023825 (2015).

[31] S. Nixon, Y. Zhu, and J. Yang, Opt. Lett. **37**, 4874 (2012).

[32] I. V. Barashenkov, L. Baker, and N. V. Alexeeva, Phys. Rev. A **87**, 033819 (2013).

[33] S. Nixon, L. Ge, and J. Yang, Phys. Rev. A **85**, 023822 (2012).

[34] K. Li and P. G. Kevrekidis, Phys. Rev. E **83**, 066608 (2011).

[35] F. K. Abdullaev, Y. V. Kartashov, V. V. Konotop, and D. A. Zezyulin, Phys. Rev. A **83**, 041805(R) (2011).

[36] N. V. Alexeeva, I. V. Barashenkov, A. A. Sukhorukov, and Y. S. Kivshar, Phys. Rev. A **85**, 063837 (2012).

[37] S. Longhi, Phys. Rev. Lett. **103**, 123601 (2009).

[38] S. Longhi, Phys. Rev. B **80**, 165125 (2009).

[39] C. T. West, T. Kottos, and T. Prosen, Phys. Rev. Lett. **104**, 054102 (2010).

[40] T. Wasak, P. Szańkowski, V. V. Konotop, and M. Trippenbach, Opt. Lett. **40**, 5291 (2015).

[41] S. Klaiman, U. Günther, and N. Moiseyev, Phys. Rev. Lett. **101**, 080402 (2008).

[42] K. Staliunas, R. Herrero, and R. Vilaseca, Phys. Rev. A **80**, 013821 (2009).

[43] Z. Lin, H. Ramezani, T. Eichelkraut, T. Kottos, H. Cao, and D. N. Christodoulides, Phys. Rev. Lett. **106**, 213901 (2011).

[44] Y. D. Chong, L. Ge, and A. D. Stone, Phys. Rev. Lett. **106**, 093902 (2011).

[45] P. Ambichl, K. G. Makris, L. Ge, Y. Chong, A. D. Stone, and S. Rotter, Phys. Rev. X **3**, 041030 (2013).

[46] V. Achilleos, P. G. Kevrekidis, D. J. Frantzeskakis, and R. Carretero-González, *Localized Excitations in Nonlinear $\mathcal{PT}$-Symmetric Systems with Defocusing Nonlinearities* (Springer, Berlin, 2014), p. 3.

[47] K. G. Makris, L. Ge, and H. E. Türeci, Phys. Rev. X **4**, 041044 (2014).

[48] K. G. Makris, Z. H. Musslimani, D. N. Christodoulides, and S. Rotter, Nat. Commun. **6**, 7257 (2015).

[49] D. N. Christodoulides, F. Lederer, and Y. Silberberg, Nature (London) **424**, 817 (2003).

[50] B. Midya, B. Roy, and R. Roychoudhury, Phys. Lett. A **374**, 2605 (2010).

[51] Z. Ahmed, Phys. Lett. A **290**, 19 (2001).

[52] M. J. Ablowitz and Z. H. Musslimani, Opt. Lett. **30**, 2140 (2005).

[53] J. Yang, J. Comput. Phys. **228**, 7007 (2009).

[54] S. Suntsov, K. G. Makris, D. N. Christodoulides, G. I. Stegeman, R. Morandotti, H. Yang, G. Salamo, and M. Sorel, Opt. Lett. **32**, 3098 (2007).

[55] S. Suntsov, K. G. Makris, D. N. Christodoulides, G. I. Stegeman, R. Morandotti, M. Volatier, V. Aimez, R. Ares, E. H. Yang, and G. Salamo, Opt. Express **16**, 10480 (2008).

[56] E. Akkermans, S. Ghosh, and Z. H. Musslimani, J. Phys. B **41**, 045302 (2008).

[57] J. Yang, *Nonlinear Waves in Integrable and Nonintegrable Systems* (SIAM, Philadelphia, 2010).

[58] L. N. Trefethen, *Spectral Methods in MATLAB* (SIAM, Philadelphia, 2000).